J. Fluid Mech. (1993), *vol.* 249, *pp.* 415–440

Direct numerical simulation of buoyancy-driven turbulence in stably stratified fluid

By THOMAS GERZ[1] AND HIDEKATSU YAMAZAKI[2]

[1] DLR, Institut für Physik der Atmosphäre W-8031 Oberpfaffenhofen, Germany

[2] Centre for Earth and Ocean Research, University of Victoria, PO Box 1700, Victoria, BC Canada, V8W 2Y2

(Received 4 November 1991 and in revised form 19 October 1992)

We investigate the role of buoyancy force on the generation and decay of random motion in a homogeneously stratified fluid by means of direct numerical simulations (DNS) of the dynamic and thermodynamic equations. The simulations start from a fluid which is at rest but has appreciable temperature fluctuations. Therefore the flow initially evolves by extracting energy from the potential energy field. Three free parameters, the Reynolds number Re, the Prandtl number Pr and the stratification number St, characterize the flow. Among these numbers the stratification number, $St = (l_{T_0}/T'_0)\,(\mathrm{d}T_R/\mathrm{d}z)$, is the most crucial one for the investigated problem. Here T'_0 and l_{T_0} are the initial r.m.s. temperature and the initial integral temperature lengthscale, respectively, and $\mathrm{d}T_R/\mathrm{d}z$ is the background stratification. St is a measure of the strength of background-temperature gradient compared to the initial mean fluctuating temperature gradient in the fluid.

A critical stratification number of order one is found to separate an oscillating, non-turbulent flow from flow states which exhibit features of turbulence. When $St > 1$, the statistics reveal a nearly linear and strongly anisotropic flow as typical for gravity waves but the flow-field variables behave randomly. When $St < 1$, i.e. when the initial gradient of fluctuating temperature exceeds the gradient of its background value, the available potential energy is sufficient to create nonlinear motions which resemble turbulence in many aspects. The properties of such a flow are a transient state of enhanced stirring and mixing, enhanced rates of dissipation of temperature fluctuations, and a quick return to isotropy.

The stratification number is an easily measurable parameter in field experiments in the ocean as well as in the atmosphere. Therefore St may be a useful indicator of whether a flow regime contains sufficient potential energy to create turbulence.

1. Introduction

The final stage of decaying turbulence is a stably stratified fluid is commonly considered as being not turbulent because the energy transfer from large to small scales is nearly zero and vertical turbulent mixing is negligible. However, it is the remnant of originally 'active' turbulent motion. Such flows often exhibit almost vanishing velocity perturbations but still detectable temperature or other scalar fluctuations and are usually referred to as 'fossil' turbulence (Woods *et al.* 1969; Nasmyth 1970; Gibson 1980). The process of 'fossilization' occurs when the molecular Prandtl number Pr of the fluid is of order one or larger (Gerz, Schumann & Elghobashi 1989; Gerz & Schumann 1991). Indeed, the existence of fossil turbulence in the oceanic thermocline where $Pr \approx 8$ is evident (e.g. Nasmyth 1970;

Munk 1981) but is also probable in air where $Pr \approx 1$ (Woods *et al.* 1969). The fossil turbulence may be frozen with respect to the mean flow (Nasmyth 1970) or may be embedded in and move with internal waves (Gibson 1980; Gerz *et al.* 1989). Although fossil turbulence has been considered as a non-mixing process, residual temperature fluctuations can create a buoyancy-driven heat flux at small scales (Gerz & Schumann 1991). In fact, during the final stage of decaying turbulence in a stratified fluid, Lange (1974) found that the density fluctuations decay faster than they would solely by molecular diffusion. This indicates enhanced mixing during the final stage. Taking these previously reported results into consideration we focus our attention on the generation and decay of turbulence by buoyancy forces. Is the potential energy merely a sink of total energy of the flow (as usually considered) or are parts of it available and, hence, can participate in mixing?

In order to investigate this problem we decided to study the onset and evolution of turbulent flow from an idealized condition. The flow will be created solely from an excess of buoyancy due to temperature fluctuations with an initially motionless state everywhere. This initial condition of our study resembles an extreme case of 'frozen fossil' turbulence (Gibson 1991). Recently, Batchelor, Canuto & Chasnov (1992) considered a similar initial-value problem, but under unstratified conditions. Sanderson *et al.* (1991) simulated active and fossil turbulence numerically but focused on differences between DNS and the direct interaction approximation. Thus, no attempt on the same subject has appeared in the literature.

The initial conditions used in our simulations are difficult to set up experimentally. Several laboratory experiments were designed in stratified salt-water tanks (e.g. Stillinger, Helland & Van Atta 1983; Itsweire, Helland & Van Atta 1986) and in thermally stratified wind tunnels (Lienhard & Van Atta 1990; Yoon & Warhaft 1990) to study the decay of grid-generated turbulence under stable stratification. Riley, Metcalfe & Weissman (1981), Métais & Herring (1989) and Gerz & Schumann (1991) considered the same type of flow numerically by means of DNS.

Because the problem is difficult to study analytically as well as experimentally, we employed the method of DNS to solve the full set of Navier–Stokes and temperature equations by computer. The DNS technique resolves all dynamically relevant scales of the fluid down to the Kolmogorov length, properly. Hence, parameterization of subgrid scale turbulence is unnecessary. This advantage is paid for by a necessarily low Reynolds number of the flow. However, Yamazaki, Osborn & Squires (1991) suggest that DNS can mimic turbulent conditions in the oceanic thermocline well. Thus, the result of our simulations may also be applicable to turbulence in the thermocline. The role of buoyancy on the dynamics of small-scale turbulence will mainly depend on the initial excess of available potential energy and on the molecular Prandtl number in the flow. Several cases will be analysed in this respect. In the next section, the method and initialization will be described. In §3 our simulation results are presented. They are discussed and compared with available laboratory data in §4. We debate the implication of our simulation in a geophysical context in §5. Our conclusions are summarized in the last section.

2. Direct numerical simulation

2.1. *Governing equations*

The three-dimensional, incompressible Navier–Stokes and temperature equations for perturbation velocities (u, v, w) or (u_1, u_2, u_3) and perturbation temperature T are integrated numerically in time and in a cubic and periodic domain with side length

L and downstream, cross-stream (spanwise) and vertical coordinates (x, y, z) or (x_1, x_2, x_3) using the Boussinesq approximation. Details of the numerical code can be found in Gerz *et al.* (1989). These equations and the continuity condition for our problem read in dimensional form

$$\frac{\partial u_i}{\partial t}+\frac{\partial}{\partial x_j}(u_j u_i) = \nu\frac{\partial^2 u_i}{\partial x_j^2}-\frac{1}{\rho}\frac{\partial p}{\partial x_i}+\alpha g T\delta_i \quad (i=1,2,3), \tag{1}$$

$$\frac{\partial T}{\partial t}+\frac{\partial}{\partial x_j}(u_j T) = \gamma\frac{\partial^2 T}{\partial x_j^2}-u_3\frac{\mathrm{d}T_\mathrm{R}}{\mathrm{d}x_3}, \tag{2}$$

$$\frac{\partial u_i}{\partial x_i}=0, \tag{3}$$

where ρ, α, g, ν, and γ represent constant values of density, volumetric expansion coefficient, gravity acceleration, kinematic viscosity, and thermal conductivity, respectively. The summation convention is used. The reference (mean) background temperature gradient $\mathrm{d}T_\mathrm{R}/\mathrm{d}z$ is linear and, hence, provides a homogeneous forcing.

2.2. *Scaling quantities and normalization*

In order to normalize the results, we define a set of reference scales (marked by an asterisk) as dimensional scaling quantities which can easily be related to measured quantities in reality. Our previous set of scaling parameters (Gerz & Yamazaki 1990) was difficult to relate to real conditions. We express the density by the constant value ρ^*, the timescale by one buoyancy period, $\tau^* = 2\pi/N^*$ (where N^* is the Brunt–Väisälä frequency), the temperature scale by the initial r.m.s.-temperature $T^* = (\overline{T_0^2})^{\frac{1}{2}} \equiv T_0'$ (where the bar denotes an ensemble, i.e. volume, average and the prime denotes the r.m.s. value). Lengths are scaled by the initial integral length of the isotropic temperature density spectrum (Hinze 1959)

$$l_\mathrm{T}^* = \tfrac{1}{2}\pi\int\frac{1}{k}S(k)\,\mathrm{d}k, \tag{4}$$

where S defines the shape of the temperature perturbation spectrum, and $k = (k_1^2+k_2^2+k_3^2)^{\frac{1}{2}}$ is the magnitude of the wavenumber vector. The velocity scales as $N^* l_\mathrm{T}^*$. With these scales of reference the normalized (non-dimensional) equations for the perturbation quantities read

$$\frac{\partial u_i}{\partial t}+\frac{\partial}{\partial x_j}(u_j u_i) = \frac{1}{Re}\frac{\partial^2 u_i}{\partial x_j^2}-\frac{\partial p}{\partial x_i}+St^{-1}T\delta_{i3} \quad (i=1,2,3), \tag{5}$$

$$\frac{\partial T}{\partial t}+\frac{\partial}{\partial x_j}(u_j T)+St\,u_3 = \frac{1}{RePr}\frac{\partial^2 T}{\partial x_j^2}, \tag{6}$$

$$\frac{\partial u_i}{\partial x_i}=0. \tag{7}$$

For simplicity, we use the same notation here as in the dimensional equations (1)–(3). We apply periodic boundary conditions in all three directions. The characterizing parameters of this system of equations are the integral-scale Reynolds number Re, the molecular Prandtl number Pr and the stratification number St which are defined as

$$Re = \frac{N^* l_\mathrm{T}^{*2}}{\nu}, \quad Pr = \frac{\nu}{\gamma}, \quad St = \frac{l_\mathrm{T}^*}{T^*}\frac{\mathrm{d}T_\mathrm{R}}{\mathrm{d}z}. \tag{8}$$

Both the Reynolds and the Prandtl numbers follow the conventional interpretation of these numbers. The stratification number is defined in analogy to the shear number in sheared flows (e.g. Gerz *et al.* 1989) and specifies the importance of fluctuating temperature for the dynamics of our system. St can be interpreted in different ways. For example, if we assume that the initial fluctuating temperature gradient scales as T^*/l_T^*, St is a measure of the strength of background-temperature gradient compared to the initial mean of fluctuating temperature gradient in the fluid. The stratification number also defines the ratio between the integral lengthscale l_T^* and the Ellison lengthscale $l_E = T^*/\mathrm{d}T_R/\mathrm{d}z$. Hence, St compares the mean size of eddies to the size of overturning eddies. A stratification number larger than one implies that the nonlinear interactions among the fluctuating quantities are small compared to the linear interactions between background stratification and perturbed flow (see (6)). For $St < 1$, the nonlinear interactions become more important and may result in a transient state of turbulence. Buoyancy effects increase in the flow with increasing inverse stratification number St^{-1} (see (5)). The Cox number Co, commonly used in the oceanography community, is the ratio of the mean square of the fluctuating temperature gradient to the square of the mean temperature gradient. In our non-dimensional system Co is inversely proportional to the square of St,

$$Co = \overline{\left(\frac{\partial T}{\partial x_i}\right)^2} St^{-2}, \tag{9}$$

where $\partial T/\partial x_i$ is the non-dimensional gradient of fluctuating temperature. Note that we consider only non-dimensional quantities for the rest of this paper.

2.3. *Initialization*

The evolution of a stratified turbulent flow is determined by the initial excess of energy available to the system. In our idealized initial condition, the velocity fluctuations and, hence, the turbulent kinetic energy $E_{kin} = \frac{1}{2}\overline{u_i^2}$, are zero. The flow will be driven exclusively from an initial excess of available potential energy, $E_{pot} = \frac{1}{2}St^{-2}\overline{T^2}$. With time, this imbalance will create E_{kin} which will be partly dissipated by viscous forces and partly retransformed into E_{pot} where thermal conductivity further extracts energy.

In this study, we keep the Reynolds number Re fixed and vary the stratification number St and the Prandtl number Pr. Different values of St result in different values for the potential energy at time zero. The data and characteristic numbers at time of initialization are summarized in table 1. Cases, A, B, C and H signify flows with $Pr = 1$ and different values for St. Cases D, E and F differ from cases A, B and C by $Pr = 2$. The same physical situation as in case E is described in case E' but the latter provides a higher resolution of the computational domain. The three-dimensional temperature perturbation field with mean value T_0' is initialized by Gaussian random numbers and obeys the prescribed spectral shape

$$S(k) = \frac{16}{2\pi}\left(\frac{2}{\pi}\right)^{\frac{1}{2}} \frac{k^4}{k_p^5} \exp\left[-2(k/k_p)^2\right], \tag{10}$$

where k is now the magnitude of the non-dimensional integer wavenumber vector and k_p is the non-dimensional peak integer wavenumber. This spectral form $S(k)$ is appropriate for the final period of decay of turbulence when the nonlinear energy transfer is small compared to the viscous dissipation. With the specifications of the spectrum (10) and the integral lengthscale (4) the initial integer peak wavenumber k_{p_0} becomes $(8\pi)^{\frac{1}{2}}$ for our computational domain size which we take as 4π.

Box length			L	4π			
Peak wavenumber			k_p	$(8\pi)^{\frac{1}{2}}$			
Turbulent kinetic energy			E_{kin}	0			
Integral-scale Reynolds number			Re	57.4			
Stratification number			St				
Prandtl number			Pr				
Temperature fluctuation			T'	0.96			
Integral length			l_T	1.0			
Potential energy			E_{pot}				
Cases	A	B	C	D	EE'	F	H
E_{pot}	0.46	7.37	0.029	0.46	7.37	0.029	1.84
St	1.00	0.25	4.00	1.00	0.25	4.00	0.50
Pr	1.0	1.0	1.0	2.0	2.0	2.0	1.0

TABLE 1. Non-dimensional data and characteristic parameters at time of initialization. The prime denotes an r.m.s. value. All simulations run with mesh 64, except case E' with mesh 128^3.

DNS requires rather low Reynolds and Prandtl numbers for proper resolution of the small velocity and temperature scales (Reynolds 1990). The values of $Re = 57.4$ for the Reynolds number and $Pr = 1$ for the molecular Prandtl number are small enough to ensure the correct resolution in a grid of mesh 64^3. Simulations with $Pr = 2$ have been performed at 64 and 128 mesh in each direction (cases E and E'). Whereas all spectra are very well resolved with 128 mesh grids, some potential energy and dissipation rate piled up at the largest resolved wavenumbers with a 64 mesh resolution and $Pr = 2$. These effects of resolution on spectral and spatial statistics will be discussed in §4.4.

Although rather small, a value of $Re \approx 60$ may still be reasonable in the oceanic thermocline (Yamazaki *et al.* 1991). However, for the selected value of Re, realistic values of the Prandtl number in the ocean ($Pr \approx 8$) are, at present, beyond the capability of available computer technology. Nevertheless, effects of a variation of small values of Pr can be studied and the results may be extrapolated to more realistic values of Pr in the ocean.

A rather large box size L relative to the integral lengthscales of turbulence is required to allow the length to grow in time without being influenced by the periodic boundaries of the domain. On the other hand, for a given resolution, L should be small enough to resolve also the smallest scales in the domain. The selected value of $L = 4\pi$ accounts for both constraints and remains unchanged for all cases A–H.

All cases have been integrated up to approximately three buoyancy periods. We used a time step of $\frac{2}{3}\Delta x, \Delta x = L/\text{mesh}$, and performed the simulations on the Cray-YMP computer at DLR, Germany. A typical run on one processor took 1160 s CPU time for 1920 timesteps.

3. Results

3.1. *Energy budgets*

The volume averaged, non-dimensional balance equations of E_{kin}, E_{pot} and the total energy $E_{tot} = E_{kin} + E_{pot}$ read for homogeneously stratified flows

$$\frac{dE_{kin}}{dt} = St^{-1}\overline{wT} - \epsilon, \quad \frac{dE_{pot}}{dt} = -St^{-1}\overline{wT} - \chi, \quad \frac{dE_{tot}}{dt} = -\epsilon - \chi, \tag{11}$$

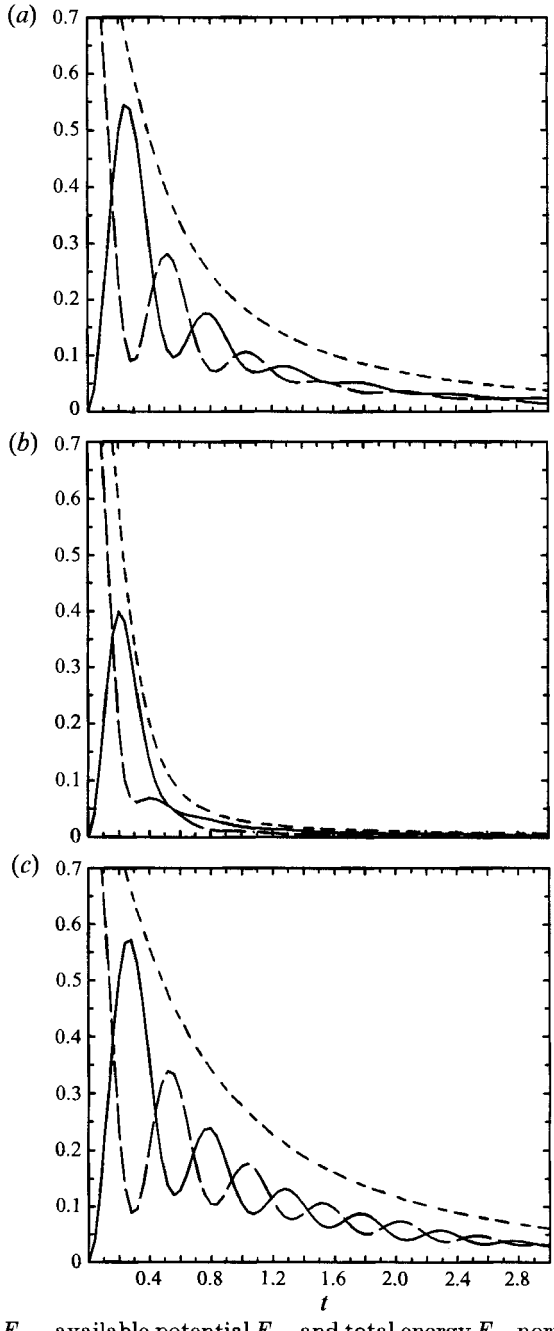

FIGURE 1. Kinetic E_{kin}, available potential E_{pot} and total energy E_{tot} normalized by the initial value E_{tot_0} *vs.* time t in buoyancy periods for (*a*) case *A*, (*b*) case *B* and (*c*) case *C*. ——, $E_{\text{kin}}/E_{\text{tot}_0}$; ——, $E_{\text{pot}}/E_{\text{tot}_0}$; – – –, $E_{\text{tot}}/E_{\text{tot}_0}$.

where
$$\epsilon = \frac{1}{Re}\overline{\left(\frac{\partial u_i}{\partial x_j}\right)^2}, \quad \chi = \frac{St^{-2}}{RePr}\overline{\left(\frac{\partial T}{\partial x_j}\right)^2} \tag{12}$$

are the dissipation rates of E_{kin} and E_{pot}, respectively. The heat flux term $\overline{wT}$ transforms energy between kinetic and available potential energy reservoirs. The rate of transformation is weighted by the inverse stratification number St^{-1}.

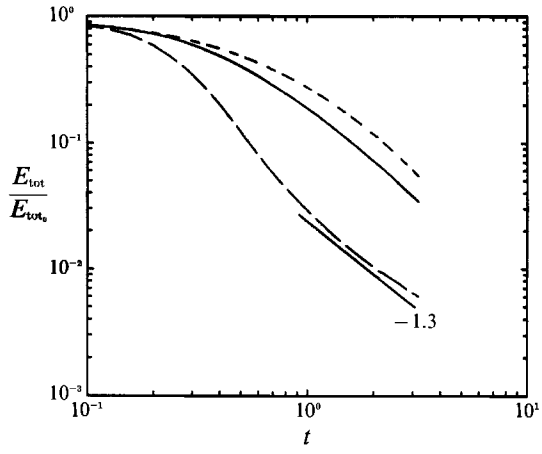

FIGURE 2. E_{tot}/E_{tot_0} *vs.* t for ——, case A; ——, case B; – – –, case C.

Figure 1 plots the temporal evolution of kinetic, potential and total energy for cases A, B and C. To emphasize the different flow evolutions we normalized the quantities by the respective initial values of the total energy. Evolutions are shown versus non-dimensional time in buoyancy periods $t = \text{time}/\tau^* = \text{time}\ (N^*/2\pi)$. According to (11), E_{pot} decays in time where the buoyancy driven motions begin and the flow gains kinetic energy E_{kin}. After approximately 0.25 buoyancy periods, E_{kin} (E_{pot}) is maximum (minimum) and the process is reversed. The total energy E_{tot} decays monotonically owing to dissipation effects. Differences between the cases show up in strength, duration and period of the oscillations of E_{kin} and E_{pot}. In case A three oscillation periods can be distinguished with $\tau_1 = \tau_2 = 0.52$ and $\tau_3 = 0.80$. In case B no full period can be resolved and case C reveals five periods with slightly decreasing intervals from $\tau_1 = 0.54$ to $\tau_{3-5} = 0.50$. The differences in the decay rates of E_{tot} between cases A, B and C are remarkable (figure 2). Whereas in cases A and C the decay rates of E_{tot} increase with time, we notice that, in case B, E_{tot} first declines rapidly until $t \approx 1.0$ and then eventually approaches a smaller decay rate of $t^{-1.3}$. This value resembles a typical decay rate of isotropic turbulence as measured in various laboratory experiments (Comte-Bellot & Corrsin 1966; Warhaft & Lumley 1978).

The dissipation rates of kinetic energy and available potential energy, ϵ and χ, for cases A, B and C evolve similarly as their respective energies (figure 3). However, χ for case B has a local minimum at $t \approx 0.08$ before it rises again to its maximum value at $t \approx 0.16$. The reason is that the initialization process provides a Gaussian distribution of the temperature fluctuations in wavenumber space. Thus, the flow field is close to linear initially and the temperature fluctuations at small scales are not fed by those at large scales. As a result, χ decreases until the nonlinearity of the flow (i.e. the energy transfer from large to small scales) is fully developed. This is the case at $t \approx 0.1$ when χ rises again. The process also happens in cases A and C and can be recognized in a slight change of the decay rate of χ.

The r.m.s. quantities of velocity and temperature are depicted in figure 4. The figure illustrates that initially the kinetic energy is predominantly stored in the vertical velocity component w. Pressure forces feed both horizontal components u and v, owing to the continuity condition. Note that all flows are perfectly isotropic in the horizontal directions, $u' = v'$, because of the flow symmetry. For cases A and

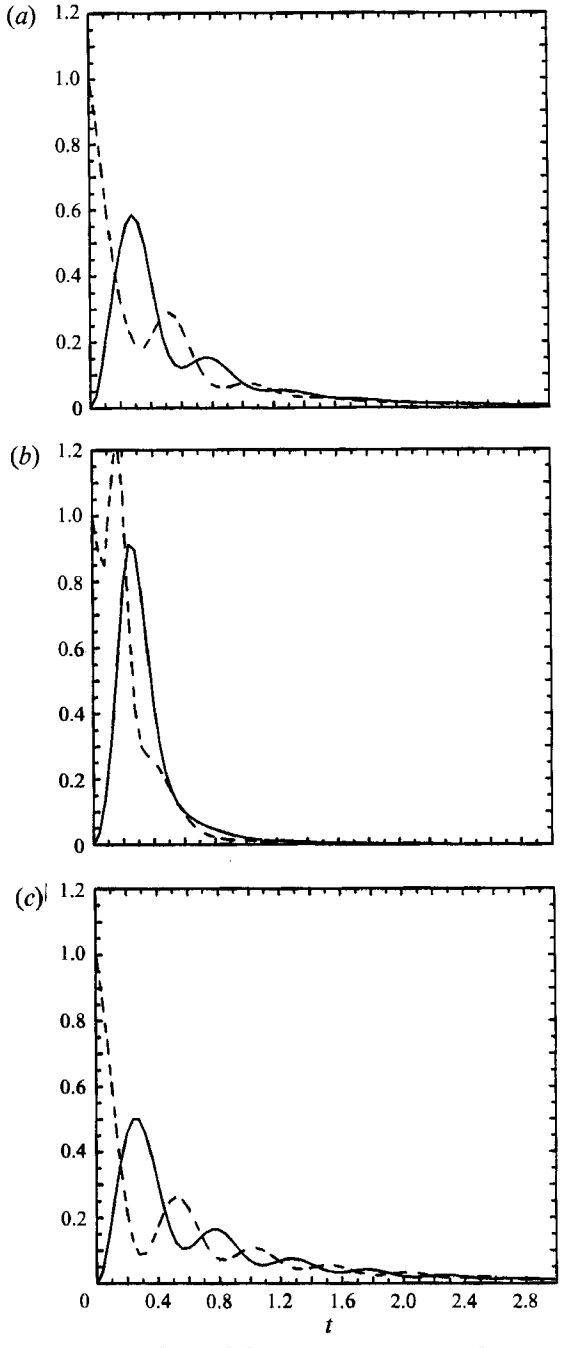

FIGURE 3. Mechanical and thermal dissipation rates, ϵ and χ normalized by χ_0, *vs.* t for (*a*) case *A*, (*b*) case *B* and (*c*) case *C*. ——, ϵ/χ_0; – – –, χ/χ_0.

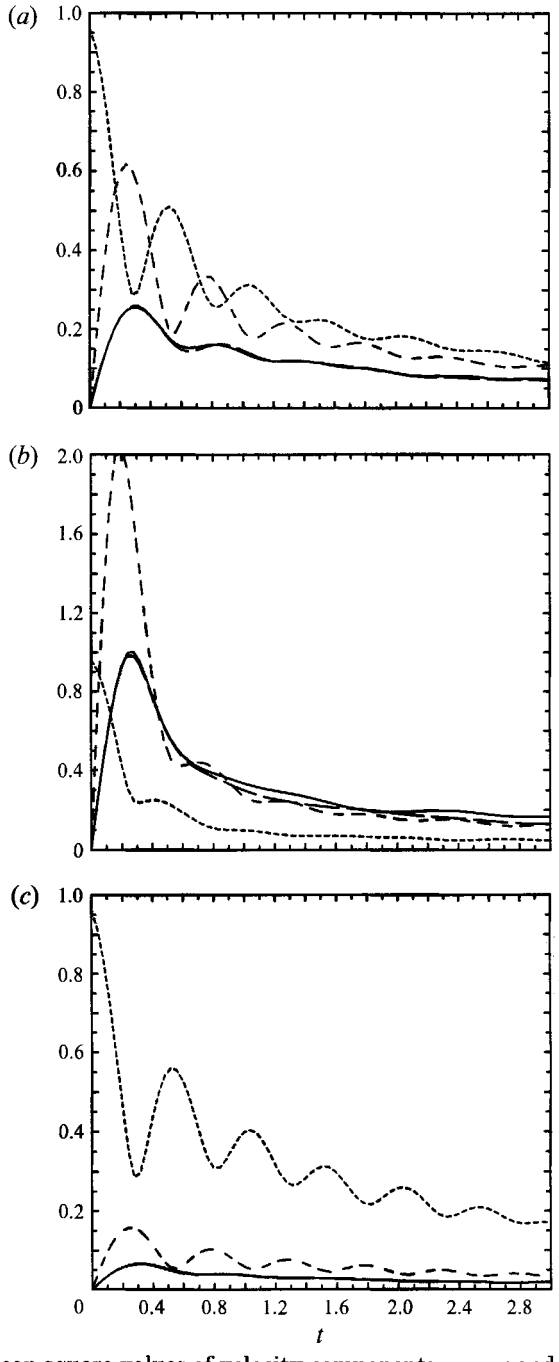

FIGURE 4. Root mean square values of velocity components u, v, w and temperature T *vs.* t for (*a*) case A, (*b*) case B and (*c*) case C. Note the different ordinate scalings. ——, u'; — —, v'; – –, w'; - - - -, T'.

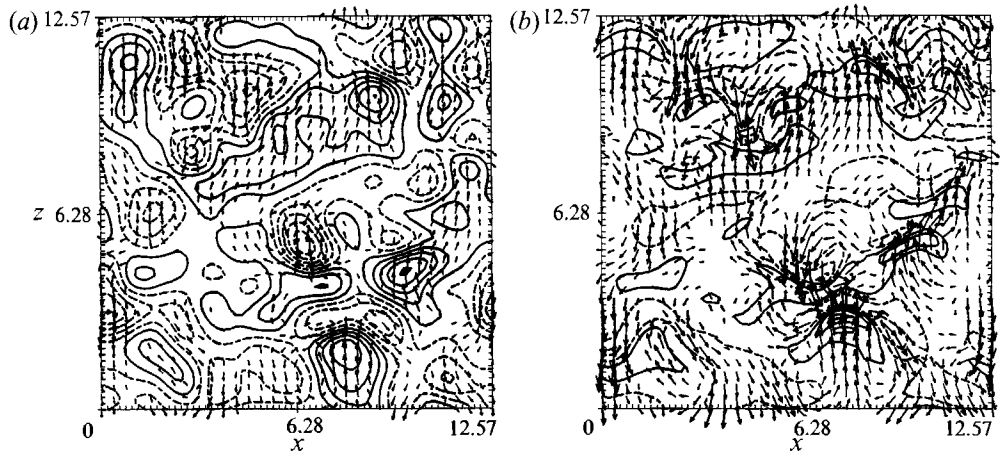

FIGURE 5. Vertical cross-sections through the instantaneous flow at cross-stream position $y = 9.42$ at times (*a*) $t = 0.08$ and (*b*) $t = 0.24$ for case A. The contours mark isovalues of the temperature perturbation field T; solid (dashed) contours indicate 'hot' ('cold') fluid between -2.7 and 2.7; the contour interval is 0.6. The arrows indicate velocity vectors (u, w) with magnitude between 0.2 and 2.

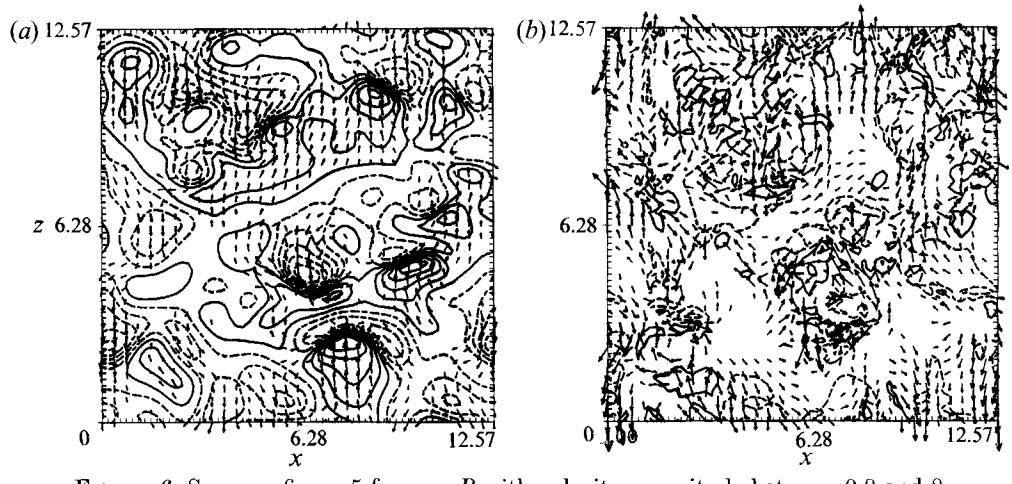

FIGURE 6. Same as figure 5 for case B with velocity magnitude between 0.8 and 8.

C we observe that u' and v' remain smaller than w' during the entire simulation period. On the other hand, for case B, u' and v' exceed w' at $t = 0.45$, and all quantities stay at about the same intensity for the rest of the time.

3.2. *Flow fields*

By means of velocity vectors (u, w) and temperature field T, instantaneous flow patterns are presented in a vertical cross-section of the domain for cases A, B and C (figures 5–7). Threshold values for the vector length differ from case to case in order to allow an easy qualitative comparison. It is obvious from the plots that at $t = 0.08$ hot fluid is moving up and cold fluid is moving down owing to pure restratification processes. The temperature isolines are compressed in the direction of parcel movements and are diluted in the 'wake' of moving parcels. This effect is strongest

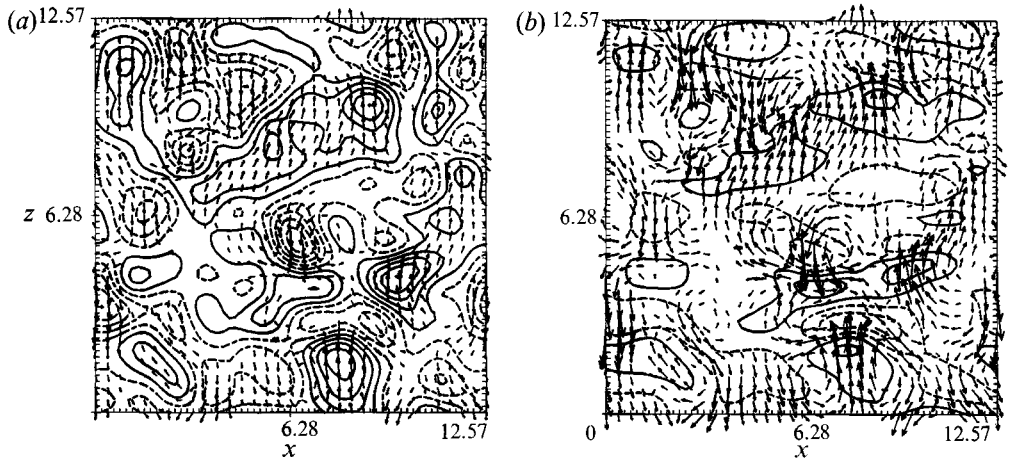

FIGURE 7. Same as figure 5 for case C with velocity magnitude between 0.05 and 0.5.

for case B and an enhanced skewness of temperature gradients is to be expected. In general, the flows look similar in all three cases at $t = 0.08$ because the simulations were started from the identical temperature perturbation field. However, at $t = 0.24$ the differences in flow behaviour of the three cases becomes more evident. Whereas cases A and C reveal almost identical flow pictures at $t = 0.08$, i.e. the flows are still buoyancy-driven and the resulting eddies last for a long time, the flow picture of case B has completely changed. The rather large upward and downward moving parcels at $t = 0.08$, giving an impression of an 'ordered' flow, have been strongly stirred at $t = 0.24$, and suggest a highly chaotic and small-scale turbulent flow state. Although the flow is stably stratified and gravity oscillations are observed in the time series of potential and kinetic energies, no plot of flow fields reveals the presence of (monochromatic) internal gravity waves.

4. Discussion

We will now discuss the simulation results presented above with respect to their differences in anisotropy, nonlinearity and spectral behaviour. The effect of increasing the Prandtl number will also be considered. We discuss the evolution of the vertical heat flux first because this quantity reflects direct effects of buoyancy.

4.1. *Vertical heat flux*

In all cases considered, the spatially averaged energy of the fluctuating flow is exchanged periodically between the reservoirs of the vertical component of the kinetic energy w' and the potential energy (or T'). The energy exchange is performed by the heat flux $\overline{wT}$ which oscillates at the same frequency around the temporal mean value of zero (figure 8). Since the kinetic energy is zero initially, the heat flux is 'counter gradient' during the early stage of flow evolution. The heat flux changes from positive to negative values when the kinetic energy is maximum (figure 1).

Second-order statistics of a purely linear flow oscillate with exactly half the buoyancy period (Hunt, Stretch & Britter 1988). The time series of E_{kin} and E_{pot} (figure 1) and of $\overline{wT}/(w'T')$ (figure 8) indeed have oscillation periods close to half the buoyancy period initially. For $t > 1.5$, the periods increase in cases A and B as a

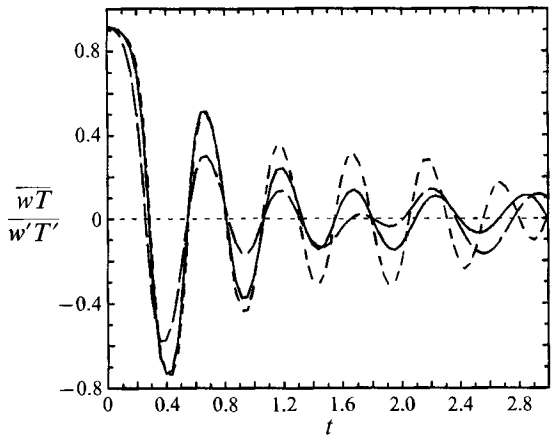

FIGURE 8. Correlation coefficient of the vertical heat flux, $\overline{wT}/(w'T')$ *vs.* t for ——, case A; ——, case B and – – –, case C.

result of nonlinear interactions among colliding fluid parcels (spectral energy transfer from large to small scales, see below). Case C is the flow with the lowest initial excess of potential energy. Therefore it exhibits only a very weak nonlinearity and the oscillation periods of second-order statistics correspond to linear flow conditions.

The results also differ with respect to the correlation-coefficient magnitude between vertical velocity and temperature perturbation at developed flow stages. Initially all cases behave similarly. At initialization, a correlation coefficient between w and T is meaningless since w is set to zero artificially, as we stated earlier. However, after the first timestep of integration every random perturbation T has created a corresponding fluctuation w according to (5). Everywhere in the domain hot fluid is ascending and cold fluid is descending. Hence, the correlation is positive and very high (Appendix). With time, the maximum correlation magnitude in each oscillation period decays since pressure forces feed the horizontal velocity components in order to satisfy mass continuity (equation (7)). The decay of the correlation coefficient is strongest for case B (weakest for case C) where we also observe large (small) dissipation rates ϵ and χ (figure 3). Again, this is due to strong (weak) nonlinear interactions among colliding fluid parcels. The strong decay of the correlation coefficient in case B also reflects the fairly strong approach to isotropy as suggested earlier. This will become more evident in the next section.

The oscillating behaviour of the flux and the strong decrease of the maximum magnitude of its correlation coefficient with time have also been reported by Lienhard & Van Atta (1990) and Yoon & Warhaft (1990). Their laboratory experiments were designed to study the decay of grid-generated turbulence in thermally stratified wind tunnels. Owing to the different initiation of turbulence compared to our studies, they observe a downgradient heat (or density) flux first which later turns into a countergradient flux when the flow restratifies. Their test sections were too short to reveal more oscillations farther downstream. An oscillation period can therefore hardly be determined. However, strong evidence for a period close to half the buoyancy period (as in our case) is provided by several numerical simulations (Riley *et al.* 1981; Métais & Herring 1989; Gerz & Schumann 1991) which used a non-zero initial kinetic energy field as the laboratory experiments.

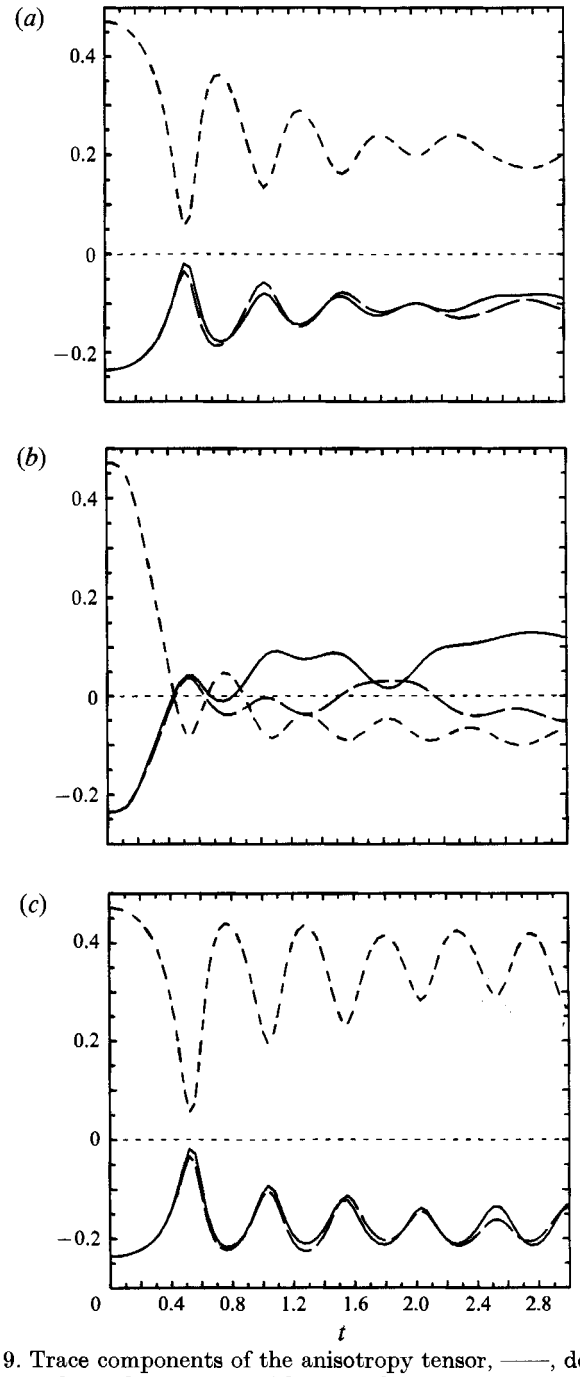

FIGURE 9. Trace components of the anisotropy tensor, ——, downstream b_{11}; ——, cross-stream b_{22} and – – –, vertical b_{33}, *vs.* t for (*a*) case A, (*b*) case B and (*c*) case C.

4.2. *Anisotropy*

We demonstrate the evolution of the anisotropy of the flow cases A, B and C by means of the trace components b_{ii} (no summation) of the anisotropy tensor,

$$b_{ij} = \frac{\overline{u_i u_j}}{2E_{\mathrm{kin}}} - \tfrac{1}{3}\delta_{ij},$$

in figure 9. Since the kinetic energy is fed by E_{pot_0} via w', the anisotropy is stored initially in the vertical component b_{33} and compensated by equal shares of the horizontal components b_{11} and b_{22}. (Note that the trace of b_{ij} must vanish.) The anisotropy after the first timestep is identical for all flows since the same initialization spectrum $S(k)$ for E_{pot_0}, equation (10), is used. With time, the anisotropy measurements in case A drop a little and oscillate with roughly half the buoyancy period around a temporally constant value of $b_{33} \approx 0.22$ and $b_{11} = b_{22} \approx -0.11$. The anisotropy of flow case C shows a temporally even increasing mean value up to 0.36 for b_{33} at $t = 3$. In both cases A and C the vertical component b_{33} is always positive, whereas other components are negative. A completely different anisotropy evolves in flow B. The anisotropy tensor components collapse between $t = 0.5$ and 1. During this period the r.m.s. velocities become almost equal, showing a consistent condition for isotropy (figure 4).

Gerz & Schumann (1991) discussed the anisotropy of a stably stratified turbulent flow (see their figure 10a) which had been initialized by exclusively kinetic energy – in contrast to our studies here. The initial kinetic energy was distributed isotropically among the velocity components. Since stable stratification suppresses vertical motions of fluid parcels, the anisotropy in their study, manifested in negative values of b_{33}, was compensated by positive horizontal components. This is just the opposite of what we observed in our buoyancy-driven flow. Clearly the initial source of the energy determines the later stage of the fraction of kinetic energy between vertical and horizontal components. However, for case B the signs of components b_{11} and b_{33} switch at about $t \approx 1.0$ and b_{11} (b_{33}) remains persistently negative (positive). Hence, for $t > 1.0$ the flow resembles the turbulence fields studied by Gerz & Schumann (1991). The vertical motion is no longer enhanced by the initial excess of E_{pot} but is suppressed owing to the stable stratification.

The flow of case B must have been strongly stirred already within half a buoyancy period after initialization. The strong stirring quickly destroys the large overturning flow structures (figure 6a) and produces small-scale turbulence which is almost isotropically distributed (figure 6b). These findings also explain the change in the decay rate of E_{tot} for flow B to $t^{-1.3}$, hence, to a rate typical for isotropic turbulence (figure 2).

4.3. *Spectral energy transfer*

One measure of nonlinearity of a flow is its spectral energy transfer. Here we consider the most energetic flow at $Pr = 1$, case B, and calculate the transfer spectra of kinetic and available potential energy according to

$$T_{\mathrm{kin}}(k,t) = \sum_{k \leqslant |k| < k+1} \hat{u}_i^* \, \hat{u}_{\mathrm{N}i} + \hat{u}_i \, \hat{u}_{\mathrm{N}i}^*, \quad T_{\mathrm{pot}}(k,t) = \frac{1}{St^2} \sum_{k \leqslant |k| < k+1} \hat{T}^* \hat{T}_{\mathrm{N}} + \hat{T} \hat{T}_{\mathrm{N}}^*.$$

The hat and the asterisk indicate the Fourier transform and the complex conjugate component, respectively. The index N denotes the nonlinear acceleration (second term of the left-hand side of (5) and (6)). The sum is taken over all wavenumber

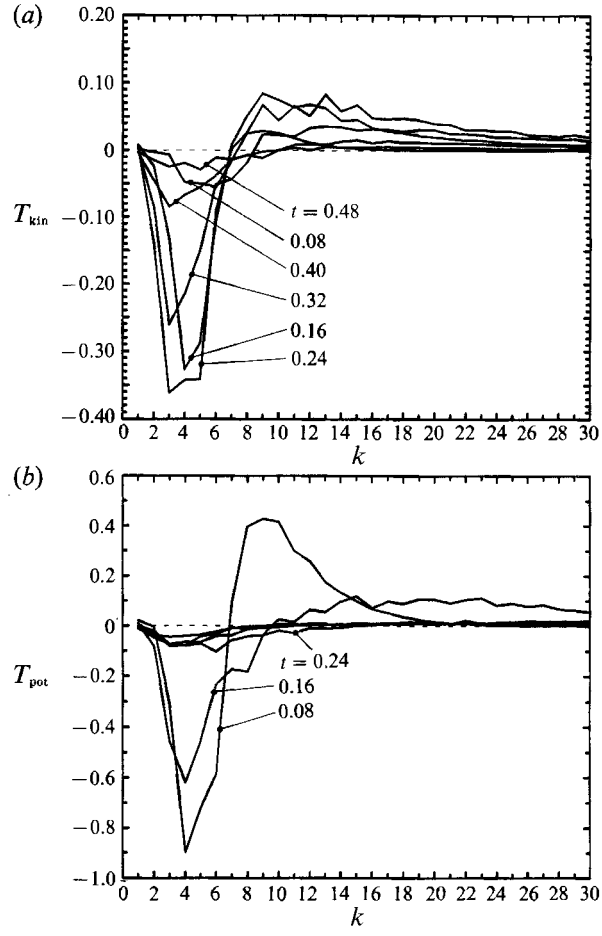

FIGURE 10. Transfer spectra of (*a*) kinetic energy T_{kin} and (*b*) potential energy T_{pot} of case *B* at times $0.08 \leqslant t \leqslant 0.48$. Note the different ordinate scaling.

vectors $\boldsymbol{k}$ which lie in a spherical shell of radius k and thickness $\Delta k = 1$. Since the spatial mean of the advective term of the energy balances vanishes in homogeneous flows, the sums of the transfer spectra $T(k)$ over all k must be zero. Hence, $T(k)$ is the net transfer rate of kinetic or potential energy within the wavenumber space. $T(k) < 0$ (> 0) describes a loss (gain) of energy at wavenumber k by nonlinear interactions.

Figure 10 depicts $T_{kin}(k)$ and $T_{pot}(k)$ at several times within the first half buoyancy period of flow *B* and reveals a net transfer from large to small scales (from small to large values of k) for both kinetic and potential energy. When the time series of χ passes the initial minimum (figure 3), the amplitude of $T_{pot}(k)$ is largest at $t = 0.08$, but $T_{kin}(k)$ is small. For $t > 0.2$ most of the potential energy is converted into kinetic energy by the vertical heat flux and T_{kin} exceeds T_{pot}. The flow evolution after $t \approx 0.5$ is characterized by an almost equal distribution of energy among the kinetic and available potential reservoirs (figure 1, case *B*) and by a smooth decay without considerable oscillations. This is also reflected in a reduced amount of spectral energy transfer rates.

Case *B* has the strongest nonlinearity of all cases considered here, owing to its highest excess of initial potential energy. A strong transfer from large to small scales

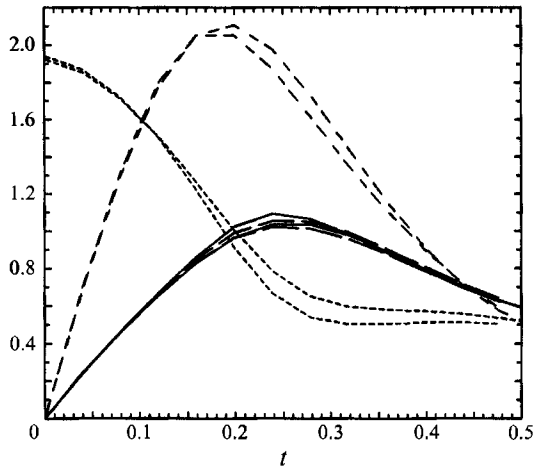

FIGURE 11. Root means square values of ——, u'; ——, v'; – – –, w'; – – –, T' *vs.* t for cases E (mesh 64^3, upper curves) and E' (mesh 128^3, lower curves).

build up quickly and vanishes again until $t \approx 0.5$. Within this interval the original features of large temperature structures are destroyed and no evidence of oscillating flow parcels exists (figure 6*b*). The plots in figure 10 also harmonize within the picture of cascading eddies since the wavenumber $k_{\text{loss/gain}}$, which divides the energy-losing wavenumber range from the energy-gaining range, increases with time. In other words, energy is transferred successively to smaller and smaller scales.

The facts and comparisons between the flow cases presented so far lead us to the conclusion that flow B reveals turbulence features in many aspects. Hence, we call it buoyancy-driven turbulence. The properties of flow B are a transient state of enhanced stirring and mixing, enhanced rates of dissipation of temperature fluctuations and a quick return to isotropy.

4.4. *Prandtl number effect*

So far we have discussed the dynamics of buoyancy-driven turbulence without the effects of the molecular Prandtl number Pr. Since one reason for the imbalance between potential and kinetic energy for decaying stratified turbulence is due to different molecular diffusivities of momentum and heat, it is reasonable to expect that a change of Pr significantly affects the dynamics of the small scales of buoyancy-driven turbulence. We attempted simulations using $Pr = 2$ for each case A, B and C with the original 64^3 mesh grid and with the same initial conditions. We call these cases D, E and F (see table 1). By increasing the Prandtl number it must be guaranteed that the temperature field is properly resolved at the smallest scales. Because case E is the most energetic case among all our simulations we performed another run E' for this case using a higher resolution of 128^3 meshes. We compare both cases with different resolutions in order to examine the effect of Pr, as well as to check the adequacy of the resolution for the other calculations, cases D and F.

Figure 11 compares the early development of r.m.s. velocity and temperature for both resolutions (cases E and E'). The resolution differences are insignificant and disappear within the first half of the first buoyancy period, $t \approx 0.5$. Higher resolution leads to a higher amount of intensity at the small scales. This enhances dissipation such that the overall effect cancels soon. Comparison of energy and dissipation rate spectra for case E with those for E' in figure 12 (*c–f*) reveals that the spectra of case

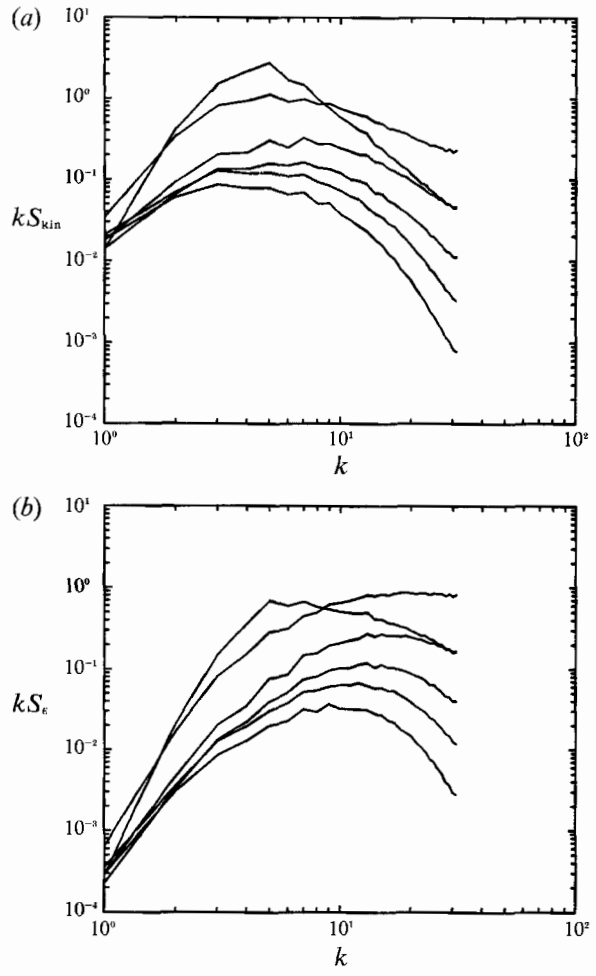

FIGURE 12(*a*, *b*). For caption see p. 433.

E' are all well resolved but that for case E small-scale potential energy piles up at high wavenumbers early. However, when the flow decays all spectra are well resolved again. Hence, we conclude that in our studies the effects of poor resolution on the flow behaviour are small and of transient nature.

We now compare the two most energetic cases B ($Pr = 1$) and E (or E', $Pr = 2$) in order to recognize the influence of an increasing molecular Prandtl number Pr on the decay of stratified turbulence. We concentrate on the spectra of the dissipation rates of kinetic energy and potential energy, $S_\epsilon(k)$ and $S_\chi(k)$, and refer to figure 13 and figure 12(*b*, *d*, *f*). Since χ is inversely proportional to Pr (see (12)), $S_\chi(k)$ becomes smaller as Pr increases. On the other hand, the remaining small-scale temperature fluctuations in case E' increase $S_\chi(k)$ at small scales. Also the dynamical dissipation rate $S_\epsilon(k)$ is increased at large wavenumbers k when Pr is increased (compare figures 13(*a*) and 12(*b*). This implies that the remaining temperature fluctuations at large k contribute to the buoyancy force and create small-scale velocity fluctuations (enhancing spectral kinetic energy $S_{kin}(k)$ at small scales) which are then dissipated. Hence, an increase in the Prandtl number increases the portion of energy which is not directly dissipated by thermal conductivity but is transformed from available

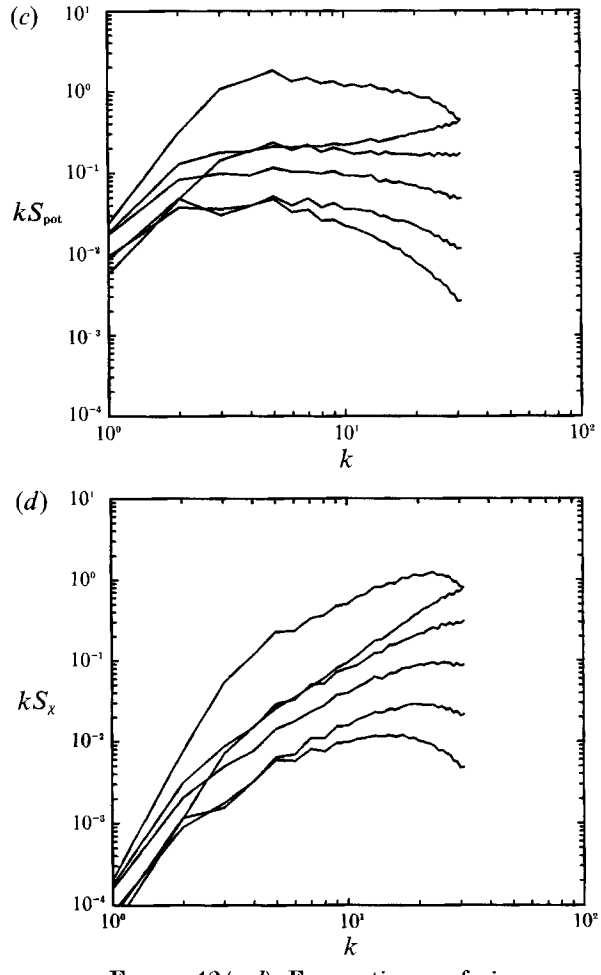

FIGURE 12 (c, d). For caption see facing page.

potential energy to kinetic energy and dissipated by molecular friction. The energy transformation is done by a small-scale heat flux which is persistently (i.e. not oscillating) counter gradient. This persistently positive heat flux at small scales is a feature of flows with Prandtl number of order one and larger (and with moderate Reynolds number) as reported by Gerz *et al.* (1989) and Gerz & Schumann (1991). Figure 14(*b*) displays the cospectrum $k \cdot C_{w\mathrm{T}}(k)$ for flow E' with $Pr = 2$ at $t = 0.16$, 0.32 and 0.48. Whereas $C_{w\mathrm{T}}(k)$ oscillates at large scales (small k) it always remains positive at small scales for $k > 15$. This effect is much weaker in flow case B with $Pr = 1$, see figure 14(*a*).

5. Implication to oceanic turbulence

Although the initial condition of our simulation hardly exists in nature, the lessons drawn from our study can be applied to oceanic turbulence. The measurement of turbulent velocity components is very difficult in comparison with scalar measurements, e.g. temperature and salinity. To date, most micro-structure experimentalists use the air-foil probe (Osborn & Crawford 1980) to measure turbulent

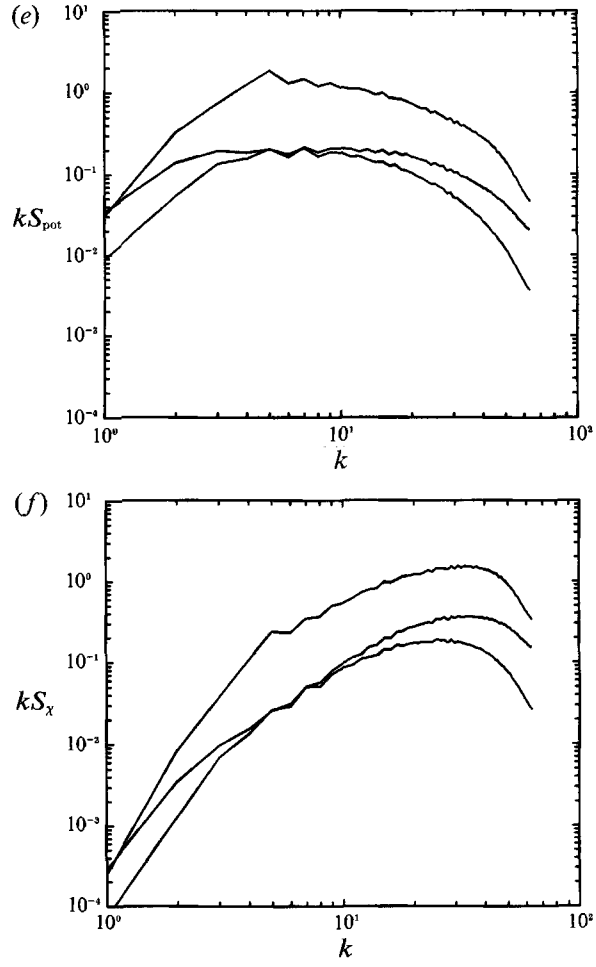

FIGURE 12. Energy and dissipation-rate spectra versus magnitude of the three-dimensional integer wavenumber vector $\boldsymbol{k}$. (*a*) kS_{kin}, (*b*) kS_ε, (*c*) kS_{pot}, and (*d*) kS_χ at times $t = 0.16$, 0.32, 0.48, 0.64, 0.80 and 0.96 (from top to bottom) for E and (*e*) kS_{pot} and (*f*) kS_χ at times $t = 0.16$, 0.32 and 0.48 (from top to bottom) for E'.

velocity components successfully. However, operating this probe requires highly skilful engineering support, and the probe has to be custom made by each experimentalist. So, only a few groups have routinely been measuring turbulent velocity components. On the other hand, fluctuating temperature is straightforward to measure using a commercially available probe. The stratification number, which we introduced in this study, plays the major role of our buoyancy-driven turbulence, and this number is only a function of 'measurable' temperature scales.

In general, fluctuating velocity associates with fluctuating temperature; thus the total energy consists of the sum of kinetic and potential energy. Here we consider that our buoyancy-driven turbulence ($St < 1$) serves a base state of stirring and mixing for a given on-going turbulent flow. Since we create a flow field from only the potential energy part of the given state (ignoring the existence of kinetic energy), it is important to know if the initial condition of the potential energy field exists in the ocean. Let us check a plausible range of the stratification number in the ocean. Both

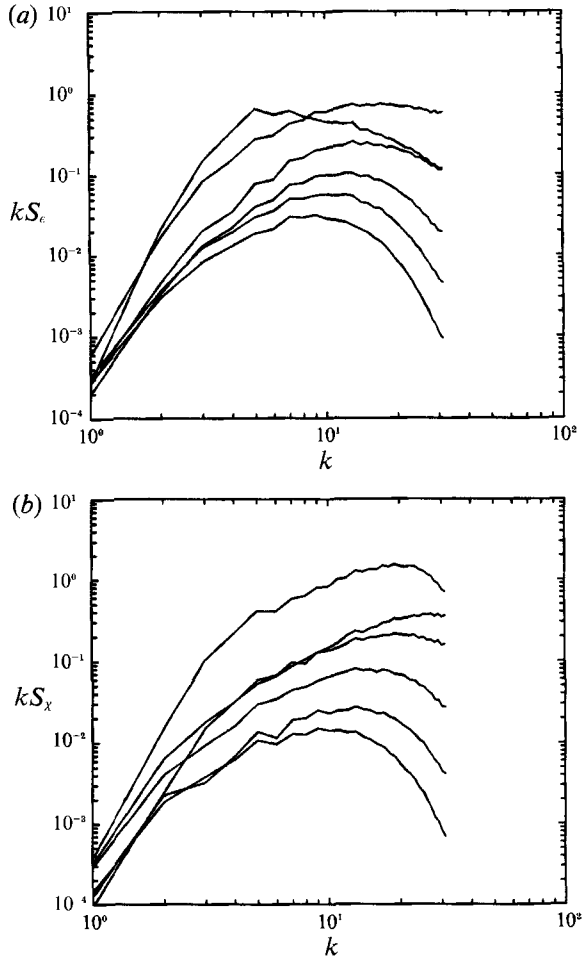

FIGURE 13. Spectra (a) kS_ε and (b) kS_χ at times $t = 0.16$, 0.32, 0.48, 0.64, 0.80 and 0.96 (from top to bottom) for case B.

r.m.s. temperature fluctuation and mean temperature gradient have been reported, e.g. Gregg (1975) and Marmorino, Dugan & Evans (1986). These quantities appear in the ranges $0.001 < T < 0.1$ (°C) and $0.001 < \mathrm{d}T_\mathrm{R}/\mathrm{d}z < 0.05$ (°C/m). Note that we do not consider a region whose fluctuating temperature is zero. Unfortunately, no integral scale of temperature has been reported so we assume this scale is in the order of magnitude of the Ozmidov length which is between 0.1 and 1 m. Then, a reasonable range for St is $0.001 < St < 50$ which illustrates that buoyancy-driven turbulence ($St < 1$) may exist in the ocean. In fact, H. Wijesekera (personal communication) performed preliminary calculations for the range of St from a recent oceanic observation data set. He found that the majority of turbulent patches appeared to show $St > 1$, but a noticeable fraction of observed turbulent patches showed $St < 1$.

Gibson (1980) proposes a hydrodynamic phase diagram to classify the state of turbulence. Although his interpretation of oceanic turbulence data is controversial, data from several laboratory and field experiments (Stillinger *et al.* 1983; Itsweire *et al.* 1986; Lienhard & Van Atta 1990; Ivey & Imberger 1991) support the fundamental idea behind the phase diagram. Yamazaki (1990) demonstrates that the finding of

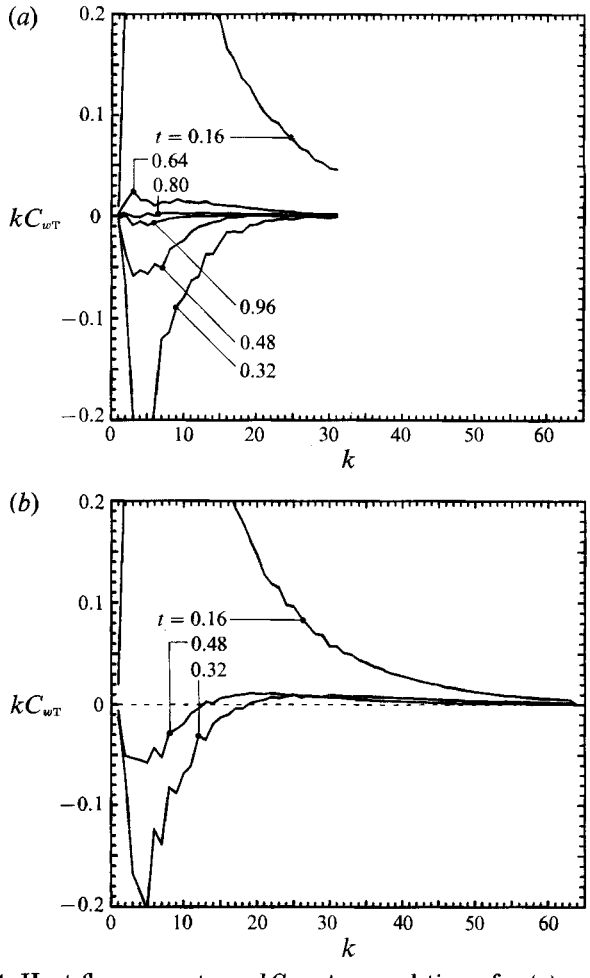

FIGURE 14. Heat-flux cospectrum kC_{wT} at several times for (*a*) case *B* and (*b*) case *E'*.

the laboratory experiments is applicable to the oceanic case. Whether the hydrodynamic phase diagram is a unique way to classify the dynamics of stratified turbulence or not, it seems worth examining the dynamics of our buoyancy-driven motions in terms of the diagram. Its abscissa is the mixing index $R = \epsilon/(\nu N^2)$ (Yamazaki 1990); the ordinate is the activity parameter defined as

$$A^2 = \frac{\epsilon}{\gamma CoN^2} = \frac{Pr}{Co} R. \tag{13}$$

Gibson's original definition of A^2 is different from our formula by a numerical factor of 13 which he deduced as a transition value $A^2_{\rm tr}$. This value marks the onset of buoyancy effects on the dynamics of turbulence. Using the criterion of significant flow departure from the passive case behaviour, Itsweire *et al.* (1986) found a transition value of $A^2_{\rm tr} = 5.5 \pm 2$ in grid-generated turbulent water ($Pr \approx 8$), but Lienhard & Van Atta (1990) and the database by Gerz & Schumann (1991) yield much larger values of 38.78 ± 0.33 and 19.3 ± 0.2, respectively, for air ($Pr \approx 1$). However, when, in order to define the onset of buoyancy effects, a criterion of 'restratification' is introduced where buoyancy length scale, w'/N, equals Ellison

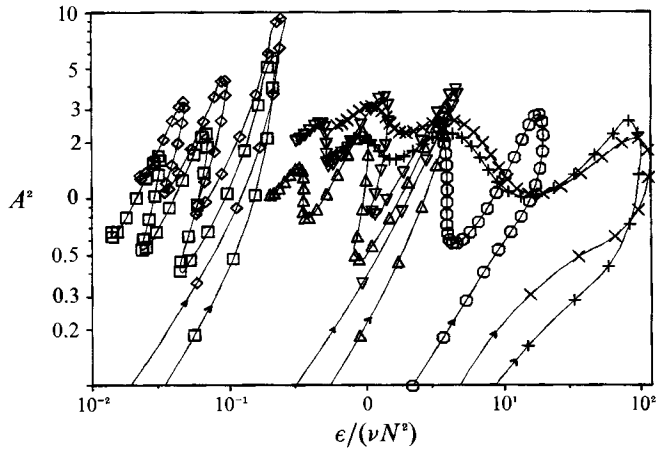

FIGURE 15. Phase diagram of all cases A–H. Activity parameter squared A^2 *vs.* $\epsilon/(\nu N^2)$ in log–log scale. $\triangle$, A; ∇, D; $+$, B; $\times$, E; $\square$, C; $\diamond$, F; $\bigcirc$, H. The arrows indicate the direction of temporal evolution of the trajectories up to $t = 1.5$.

lengthscale, $T^*/(\mathrm{d}T_R/\mathrm{d}z)$, Lienhard & Van Atta (1990) find a value of 6.18 ± 0.29. With this criterion a similar value of $A_{tr}^2 = 6.1 \pm 0.3$ can be deduced from the database by Gerz & Schumann. A further discussion of the transient values can be found in Itsweire *et al.* (1990).

The transient dissipation rate $\epsilon_{tr} = R_{tr}\,\nu N^2$ is defined as the value at which the mean vertical density flux is zero the first time ('extinction of turbulence'). The value of the transient mixing index ratio $R_{tr} \approx 16$ has become a popular tool to argue mixing due to turbulence. Itsweire *et al.* (1986) measured $R_{tr} \approx 15$ or 21 depending on the size of the turbulence-generating grid in their water channel. Lienhard & Van Atta (1990) report a value of 8.7 in the wind tunnel. Gerz & Schumann's (1991) data indicate a value of $R_{tr} \approx 8$ in their shear flows. Gibson (1980) predicts a value of $R_{tr} = 30$.

Figure 15 displays the trajectories for all seven cases of our simulations in the hydrodynamic phase diagram. Owing to the lack of kinetic energy initially, all trajectories start at the origin of the diagram. All flows have activity parameters which are below the reported transient values, although they are very close to some of them. Gibson's value of $A_{tr} = 13$ has been deduced under the assumption of the existence of a universal inertial subrange of turbulence. Our flows do not exhibit such a subrange owing to the small value of Re. Figure 15 also reveals that the most energetic cases B, E and H exceed the reported transient dissipation rates during early evolution periods.

We notice that with increasing initial potential energy and Prandtl number the dynamic range of both R and A^2 expands. Flows with stratification number less than one (cases H, B and E) exhibit the largest dynamic range in terms of R. Flows with stratification number larger than one (cases C and F) exhibit the largest range in terms of A^2. We notice further that the mixing index is rather insensitive for variations in Pr but increasing with St^{-1}, i.e. growing buoyancy influence (see, from left to right, trajectories of cases C, A, H, B for $Pr = 1$ and F, D, E for $Pr = 2$). The activity parameter oscillates around a mean value of around 1.5. A decreasing St^{-1} enhances the elongations of the oscillations and results in sharper angles of the trajectories, reflecting the oscillatory behaviour of increasingly linear fluctuations. Hence, the smoothness of the trajectory in the hydrodynamic phase diagram is

clearly related to the strong non-linearity of the dynamics. A^2 is enhanced when Pr increases but the growth rate is less than (13) suggests. All together, from (13) we learn that the increase of R with St^{-1} must be over-compensated by an increase of Co, whereas the increase of Pr must partly be compensated by growing Co.

6. Conclusion and summary

In order to identify the role of buoyancy forces during the final stage of decay of stratified turbulence, we studied the onset and decay of buoyancy-driven motions in a stably stratified fluid and adopted an idealistic 'frozen fossil' (Gibson 1991) turbulence state as the initial condition of our direct numerical simulation. In reality, this type of buoyancy-driven motion will be initiated before decaying turbulence reaches the state of our initial condition. However, our simulations demonstrate that an excess of potential energy may occasionally create a transient state of turbulence in which enhanced stirring and mixing is observed.

Buoyancy-driven flows can be characterized by three free parameters, Re, Pr and St. Among these numbers the stratification number, St, is the most crucial for our system.

Our results are summarized as follows:

1. When $St < 1$, hence, when the initial gradient of fluctuating temperature exceeds the gradient of background temperature, the available potential energy creates an energetic motion which points to some typical features of turbulence. During an early phase the flow exhibits strong nonlinearity in the energy transformation and approaches quickly towards an isotropic state. One of the most striking phenomena we found from this type of buoyancy-driven flow is the enhanced rate of dissipation of temperature fluctuation. Particularly during the first half of the buoyancy period, a collision of oppositely moving warm and cold blobs of fluid (figure 6) creates an elevated temperature gradient and accelerates the dissipation of temperature fluctuations (figure 3). As a result, the total energy reduction is also enhanced.

2. On the other hand, when $St > 1$, hence, when the background-temperature gradient is stronger than the fluctuating gradient, the available potential energy is too weak to create turbulence. The flow remains in an oscillating state with large and even increasing anisotropy. The statistics exhibit a nearly linear process, but still detectable nonlinearity exists in the flow-field variables. Although the symptom of the flow is indistinguishable from linear internal gravity waves (see e.g. the vertical heat-flux correlation coefficient in figure 8), the visualization of the flow fields (figures 5 and 7) indicates that it is different from the conventional picture of internal waves. The flow appears rather as a field of randomly distributed oscillating pendulums.

3. The effect of the molecular Prandtl number on the flow evolution is such that increasing Pr increases the turbulent kinetic energy of the flow since the portion of E_{pot} which is not directly dissipated by thermal conductivity but is transformed into turbulent motion is augmented. The transformation is done by a persistently positive small-scale heat-flux. Thus, an increasing Prandtl number will emphasize the effect of buoyancy-driven turbulence.

Finally, we note that because the stratification number is a measurable parameter in a field experiment such as oceanic turbulent measurements, it is useful to check whether the available potential energy is sufficient to create turbulence, i.e. $St < 1$. Stratification numbers smaller than one may be achieved by a change in the background stratification owing to coexisting flow conditions such as large-scale

oscillations and small-scale turbulence. For example, when a Kelvin–Helmholtz billow detaches vertically from a strongly stratified layer into a weakly stratified layer (e.g. by shear), a sudden change from kinetic to potential energy is expected. The apparent temperature fluctuation T is elevated in the weak stratification; the mean temperature gradient is low. Hence, both parameters act to reduce St. What role the stratification number plays in the mixing process is an increasing oceanographic question.

Appendix

We derive the value of the correlation coefficient $\overline{wT}/(w'T')$ for small times, i.e. when $t \to 0$ (§4.1). Then we can neglect nonlinear terms and molecular forces in (5) and (6) but we have to consider pressure effects (J. Chasnov, personal communication), since any vertical motion created by buoyancy will produce horizontal motions instantaneously in an incompressible and quite fluid. At $t = 0$, $w = 0$ but $T = T_0$ is non-zero and approximately constant. Hence, for small times we yield the approximate solutions in wavenumber space (including pressure gradient)

$$w \approx t St^{-1} T_0 (1 - k_z^2/k^2), \quad T \approx T_0.$$

For convenience we transform the equation for w into a spherical coordinate system (k, θ, ϕ) with $k_z = k \cos\theta$ and get

$$w \approx t St^{-1} T_0 \sin^2\theta.$$

Multiplying w with T and volume-averaging we yield

$$V\overline{wT} \approx \iiint t St^{-1} T_0^2 \sin^2\theta\, k^2 \sin\theta \,\mathrm{d}k\,\mathrm{d}\theta\,\mathrm{d}\phi = t St^{-1} T_0^2 \tfrac{8}{9}\pi k^3,$$

where V is the volume of a sphere with a given k. Similarly we obtain

$$V\overline{ww} \approx \iiint (t St^{-1} T_0)^2 \sin^4\theta\, k^2 \sin\theta \,\mathrm{d}k\,\mathrm{d}\theta\,\mathrm{d}\phi = (t St^{-1} T_0)^2 \tfrac{32}{45}\pi k^3,$$

$$V\overline{TT} \approx \iiint T_0^2 k^2 \sin\theta \,\mathrm{d}k\,\mathrm{d}\theta\,\mathrm{d}\phi = T_0^2 \tfrac{4}{3}\pi k^3.$$

Hence, the heat-flux correlation-coefficient is

$$\frac{\overline{wT}}{(\overline{wwTT})^{\frac{1}{2}}} = \frac{\frac{8}{9}\pi k^3}{(\frac{32}{45}\pi k^3 \cdot \frac{4}{3}\pi k^3)^{\frac{1}{2}}} = (\tfrac{5}{6})^{\frac{1}{2}} \approx 0.913.$$

This analytical value which has also been reported by Batchelor *et al.* (1992) is very close to the value of 0.914 obtained from our numerical simulations (figure 8).

We acknowledge the comments made by U. Schumann, C. Gibson, J. Chasnov and an anonymous referee. We are also grateful to H. Wijesekera for providing unpublished oceanic data for the stratification number.

This work was supported by ONR Grant no. N00014-91-J-1319.

REFERENCES

Batchelor, G. K., Canuto, V. M. & Chasnov, J. R. 1992 Homogeneous buoyancy-generated turbulence. *J. Fluid Mech.* **235**, 349–378.

Comte-Bellot, G. & Corrsin, S. 1966 The use of contraction to improve the isotropy of grid-generated turbulence. *J. Fluid Mech.* **25**, 657–682.

Gerz, T. & Schumann, U. 1991 Direct simulation of homogeneous turbulence and gravity waves

in sheared and unsheared stratified flows. In *Turbulent Shear Flow 7* (ed. F. Durst *et al.*), pp. 27–45. Springer.

GERZ, T., SCHUMANN, U. & ELGHOBASHI, S. E. 1989 Direct numerical simulation of stratified homogeneous turbulent shear flows. *J. Fluid Mech.* **200**, 563–594.

GERZ, T. & YAMAZAKI, H. 1990 Mixing during the final stage of decay of turbulence in stably stratified flow. *Proc. 9th Conf. on Turbulence and Diffusion, April 30–May 3, 1990, Roskilde, Denmark*, pp. 393–396.

GIBSON, C. H. 1980 Fossil temperature, salinity and vorticity turbulence in the ocean. In *Marine Turbulence* (ed. J. Nihoul), pp. 221–257, Elsevier Oceanography Series.

GIBSON, C. H. 1991 Laboratory, numerical and oceanic fossil turbulence in rotating and stratified flows. *J. Geophys. Res.* **96**, C 7, 12549–12566.

GREGG, M. C. 1975 Microstructure and intrusions in the California current. *J. Phys. Oceanogr.* **5**, 253–278.

HINZE, J. O. 1959 *Turbulence*, p. 227. McGraw-Hill.

HUNT, J. C. R., STRETCH, D. D. & BRITTER, R. E. 1988 Length scales in stably stratified turbulent flows and their use in turbulence models. In *Stably Stratified Flows and Dense Gas Dispersion* (ed. J. S. Puttock), pp. 285–321. Clarendon.

ITSWEIRE, E. C., HELLAND, K. N. & VAN ATTA, C. W. 1986 The evolution of grid-generated turbulence in a stably stratified fluid. *J. Fluid Mech.* **162**, 299–338.

ITSWEIRE, E. C., HOLT, S. E., KOSEFF, J. R. & FERZIGER, J. H. 1990 Direct numerical simulation of stably-stratified sheared turbulence: implications for oceanic mixing. *Center of Turbulence Research, Proc. of the Summer Program 1990, Stanford*, pp. 163–180.

IVEY, G. N. & IMBERGER, J. 1991 On the nature of turbulence in a stratified fluid. Part I: The energetics of mixing. *J. Phys. Oceanogr.* **21**, 650–658.

LANGE, R. E. 1974 Decay of turbulence in stratified salt water. Ph.D thesis, University of California at San Diego.

LIENHARD V., J. H. & VAN ATTA, C. W. 1990 The decay of turbulence in thermally stratified flow. *J. Fluid Mech.* **210**, 57–112.

MARMORINO, G. O., DUGAN, J. P. & EVANS, T. E. 1986 Horizontal variability of microstructure in the vicinity of a Sargasso sea front. *J. Phys. Oceanogr.* **16**, 967–980.

MÉTAIS, O. & HERRING, J. R. 1989 Numerical simulations of freely evolving turbulence in stably stratified fluids. *J. Fluid Mech.* **202**, 117–148.

MUNK, W. H. 1981 Internal waves and small-scale processes. In *Evolution of Physical Oceanography* (ed. B. A. Warren & C. Wunsch), pp. 264–291. MIT Press.

NASMYTH, P. W. 1970 Ocean turbulence. PhD thesis, University of British Columbia, Vancouver, Canada, 69 pp.

OSBORN, T. R. & CRAWFORD, W. R. 1980 An airfoil probe for measuring turbulent velocity fluctuation in water. Air–Sea Interaction: Instruments and Methods (ed. F. Dobson, L. Hase & R. Davis). Plenum.

REYNOLDS, W. C. 1990 The potential and limitations of direct and large eddy simulations. In *Whither Turbulence? Turbulence at the Crossroads* (ed. J. L. Lumley). Lecture Notes in Physics, vol. 357, 313–343. Springer.

RILEY, J., METCALFE, R. & WEISSMAN, M. 1981 Direct numerical simulations of homogeneous turbulence in density-stratified fluids. In *Nonlinear Properties of Internal Waves* (ed. B. J. West), *AIP Conf.* vol. 76, pp. 79–112.

SANDERSON, R. C., LEONARD, A. D., HERRING, J. R. & HILL, J. C. 1991 Fossil and active turbulence. In *Turbulence and Coherent Structures* (ed. O. Métais & M. Lesieur), pp. 429–448.

STILLINGER, D., HELLAND, K. & VAN ATTA, C. 1983 Experiments on the transition of homogeneous turbulence to internal waves in a stratified fluid. *J. Fluid Mech.* **131**, 91–122.

WARHAFT, Z. & LUMLEY, J. L. 1978 An experimental study of the decay of temperature fluctuations in grid-generated turbulence. *J. Fluid Mech.* **88**, 659–684.

WOODS, J. D., HÖGSTRÖM, V., MISME, P., OTTERSTEN, H. & PHILLIPS, O. M. 1969 Fossil turbulence. *Radio Science* **4**, 1365–1367.

YAMAZAKI, H. 1990 Stratified turbulence near the critical dissipation rate. *J. Phys. Oceanogr.* **20**, 1583–1598.

YAMAZAKI, H., OSBORN, T. R. & SQUIRES, K. D. **1991** Direct numerical simulation of planktonic contact in turbulent flow. *J. Plankton Res.* **13**, 629–643.

YOON, K. & WARHAFT, Z. **1990** The evolution of grid-generated turbulence under conditions of stable thermal stratification. *J. Fluid Mech.* **215**, 601–638.